# Physical mechanisms driving the global ocean breathing

Esther Portela Rodriguez[1], Nicolas Kolodziejczyk[2], Virginie Thierry[3], and Clément Vic[2]

[1]LOPS, CNRS
[2]Univ. Brest
[3]Ifremer

November 22, 2022

**Abstract**

Future changes in subduction are suspected to be critical for the ocean deoxygenation pre- dicted by climate models over the 21 st century. However, the drivers of global oxygen subduction have not been fully described or quantified. Here, we address the physical mech- anisms responsible for the oxygen transport across the late winter mixed layer base and their relation with water-mass formation. Up to 70% of the global oxygen uptake takes place during Mode Water subduction mostly in the Southern Ocean and the North At- lantic. This oxygen subduction is driven by the combination of strong currents with large mixed-layer-depth gradients at localized hot-spots and by the wind-driven vertical velocity within the Subtropical gyres. Although oxygen diffusion, often neglected, is uncertain, it is likely to be important for the global oxygenation. The physical mass flux dominates the total oxygen subduction while the oxygen solubility plays a minor role in its modulation.

# Physical mechanisms driving the global ocean breathing

**Esther Portela[1]*, Nicolas Kolodziejczyk[1], Virginie Thierry[1]and Clément Vic[1]**

[1]Univ. Brest, CNRS, IRD, Ifremer, Laboratoire d'Oceanographie Physique et Spatiale (LOPS), Plouzane, France

**Key Points:**

- Up to 70% of the global oxygen uptake occurs during Mode Water subduction,driven by lateral induction and vertical velocity.
- Oxygen diffusion, despite large uncertainties, is likely to play an important role in the global oxygen uptake.
- Total oxygen subduction is driven by the mass flux, with little contribution of the latitudinal variability of the $[O_2]$.

Corresponding author: Esther Portela, eportelanh@gmail.com

## Abstract

Future changes in subduction are suspected to be critical for the ocean deoxygenation predicted by climate models over the $21^{st}$ century. However, the drivers of global oxygen subduction have not been fully described or quantified. Here, we address the physical mechanisms responsible for the oxygen transport across the late winter mixed layer base and their relation with water-mass formation. Up to 70% of the global oxygen uptake takes place during Mode Water subduction mostly in the Southern Ocean and the North Atlantic. This oxygen subduction is driven by the combination of strong currents with large mixed-layer-depth gradients at localized hot-spots and by the wind-driven vertical velocity within the Subtropical gyres. Although oxygen diffusion, often neglected, is uncertain, it is likely to be important for the global oxygenation. The physical mass flux dominates the total oxygen subduction while the oxygen solubility plays a minor role in its modulation.


## 1 Introduction

A global ocean deoxygenation trend has been observed over the past decades and it is predicted by climate models to increase over this century (Helm et al., 2011; Schmidtko et al., 2017; Keeling & Garcia, 2002; Keeling et al., 2010; Ito et al., 2017; Oschlies et al., 2018; Bopp et al., 2002, 2013). This decrease in the global ocean oxygen concentration ($[O_2]$) has been attributed to the warming climate operating directly via the decrease of oxygen solubility and indirectly by an increased stratification and changes in respiration and ventilation (Oschlies et al., 2018; Schmidtko et al., 2017). Ocean ventilation refers to the combination of processes by which the surface waters that have been recently in contact with the atmosphere are injected into the ocean interior (like kinematic and diffusive subduction) (Cushman-Roisin, 1987; Qiu & Huang, 1995; Marshall et al., 1993) and transported away from their sources (interior circulation and mixing) (Naveira Garabato et al., 2017; Luyten et al., 1983).

Reduced ventilation has been proposed as the main mechanism driving the ongoing global oxygen loss (Helm et al., 2011; Keeling et al., 2010; Keeling & Garcia, 2002; Long et al., 2016). However, the different ventilation processes have not been fully unraveled or quantified. On decadal timescales, the strongest negative oxygen trends have been detected in the least ventilated regions with an associated expansion of the oxygen minimum zones (Stramma et al., 2008; Schmidtko et al., 2017; Helm et al., 2011), while newly subducted water masses do not show a detectable deoxygenation signal (Oschlies et al., 2018; Schmidtko et al., 2017; Helm et al., 2011). These patterns suggest that oxygen loss over the past decades is consistent with a reduced interior transport and the overturning circulation slowdown (Schmidtko et al., 2017; Brandt et al., 2015; Oschlies et al., 2018). In contrast, a recent climate model simulation has shown a major contribution of a reduced subduction to the long-term oxygen loss, suggesting that changes in location and intensity of subduction are critical to understand the long-term deoxygenation (Couespel et al., 2019).

Oxygen can be brought into the ocean interior through water mass formation at high latitudes and released back into the mixed layer (ML) in zones of strong upwelling (Liu & Huang, 2012). However, the mechanisms setting the relationship between these ventilation regions and the associated water masses are still poorly understood at global scales.

In the context of climate change, given the importance of the subduction process for the present and future of the oceanic oxygen content, it is crucial to understand and quantify the global oxygen subduction ($S^{ox}$). We focus on the relative contribution of the physical mechanisms driving the oxygen uptake and release by the interior ocean, i.e. the global ocean breathing.

## 2 Key concepts on oxygen subduction

There are three competing processes driving the global ocean oxygen inventory: (i) the air/sea transfer tied to oxygen solubility (Koelling et al., 2017), mainly controlled by the seawater temperature, (ii) the $S^{ox}$ that carries the oxygen-rich surface waters to the ocean interior (Cushman-Roisin, 1987; Marshall et al., 1993) and (iii) the biological respiration and remineralization (Resplandy, 2018; Wyrtki, 1965). Within the ML, $[O_2]$ is, to first order, in equilibrium with the atmosphere and therefore close to 100% saturation ($O_{sat}$), deviations from saturation are usually found in deep convection zones (Koelling et al., 2017).

In Figure 1 we illustrate the oxygen subduction/obduction process and their effect on the interior $[O_2]$ ($[O_2]_i$) and oxygen inventory. The ML is considered as a buffer between the atmosphere and the ocean interior. Oxygen obduction ($O^{ox}$) is defined here as the opposite of subduction, i.e. the oxygen flux from the permanent thermocline through the steady, late winter ML base into the seasonal thermocline/ML (Sallée et al., 2012, 2010; Marshall et al., 1993; Kwon et al., 2016). To isolate the subduction effect, for simplicity, in this conceptual schematic we set a steady oxygen solubility in the ML and a constant respiration in time and space. While biogeochemical processes are important to modulate the $[O_2]$ in certain regions (Richardson & Bendtsen, 2017), they are beyond the scope of this study.

Putting aside the effect of biogeochemical processes, the $S^{ox}$ increases the oxygen inventory within a given volume delimited by the late winter ML base and an isopycnal surface ($\sigma_n$). This is due to the volume augmentation and to the uptake of well oxygenated waters with $[O_2] \approx O_{sat}$ by the interior ocean. Since $O_{sat}$ is usually higher than $[O_2]_i$, this process also increases $[O_2]_i$.

In an obductive location, the oxygen inventory decreases due to a negative mass flux. However, this flux alone will not change the $[O_2]$ of the given volume ($\Delta[O_2]_i = 0$, Figure 1b). In the ML, the $[O_2]$ ($[O_2]_{ml}$) decreases due to the mixing of nearly saturated with interior, less oxygenated waters. However, due to the air-sea equilibrium, the $[O_2]_{ml}$ rapidly re-saturates (few days for a ML of 50 m (Gruber et al., 2001)). Note that oxygen diffusion can take place in a net obductive location where it would increase the local $[O_2]_i$. However, the kinematic mass and oxygen flux to the mixed layer would overwhelm this effect. As in the global ocean mass must be conserved, the obduction and subduction mass flux must compensate each other. This implies that $S^{ox}$ is the only dynamical mechanism able to increase the global $[O_2]_i$. The subsequent water-mass mixing and spreading do not change the global oxygen inventory, but they drive the oxygen distribution over the entire ocean at interannual to decadal timescales (Joos et al., 2003).

## 3 Methods

### 3.1 Oxygen Subduction Computation

While the ML depth varies seasonally with the resulting entrainment/detrainment of water, permanent subduction (in contrast with the instantaneous subduction first described by Cushman-Roisin (1987)) accounts for the fraction of water that has irreversibly entered the permanent thermocline across the steady late-winter ML base ($H_{max}$) (Donners et al., 2005; Marshall et al., 1993). This permanent $S^{ox}$ is determined by the mass flux across $H_{max}$ carrying the measured oxygen (kinematic subduction) and by the turbulent oxygen diffusion due to the difference in $[O_2]$ in the ML/seasonal thermocline and the ocean interior. Its net value (positive into the ocean interior and negative into the thermocline) is the sum of the contributing terms that are expressed as follows (Sallée et al., 2012):

$$\overline{S^{ox}} = \underbrace{\overline{[O_2]} \cdot \overline{U} \cdot \nabla_h \overline{H_{max}}}_{\text{Lateral induction}} + \underbrace{\overline{[O_2]} \cdot \nabla_h (\overline{U^* H_{max}})}_{\text{Eddy-induced}} + \underbrace{\overline{[O_2]} \cdot \overline{w}}_{\text{Vertical}} + \underbrace{k_v \cdot \nabla_v \overline{[O_2]_h} + k_h \cdot \nabla_h \overline{[O_2]_h} \cdot \nabla_h \overline{H_{max}}}_{\text{Diffusion}} \quad (1)$$

Where $U$ and $U^*$ are respectively the horizontal mean and bolus velocity fields, $w$ is the vertical velocity and $\nabla_h$ is the horizontal divergence operator. $U^*$, represents the advective contribution of unresolved eddies (Forget et al., 2015) parametrized following (Gent & McWilliams, James, 1990). Vertical diffusion in the ocean interior is mainly driven by turbulent mixing induced by the breaking of internal tides (Munk & Wunsch, 1998). Hence, we use a geographically-variable vertical diffusion coefficient $k_v$ based on a parametrisation of tidally-driven mixing (de Lavergne et al., 2020). $k_v$ is determined at the base of the mixed layer as $k_v = 0.2\varepsilon/N^2$ (Osborn, 1980), where $\varepsilon$ is the turbulent energy dissipation and $N^2$ is the buoyancy frequency.

Based on previous studies, the lateral diffusion coefficient is set to be $k_h = 10^3 m^2 s^{-1}$ (Köhl et al., 2007; Forget et al., 2015) but this coefficient is spatially variable (Klocker & Abernathey, 2014; Abernathey & Marshall, 2013) and uncertain as it is based in parametrisations that depend on the dataset resolution. To discuss the potential role of diffusion on the global oxygen uptake we have computed it with the lower and higher $k_h$ boundaries ($k_h = 10^2 - 10^4 m^2 s^{-1}$, (Forget et al., 2015)). Here, we examine mean $S^{ox}$ from monthly climatological fields (overbars in 1) and the resulting mean $S^{ox}$ is the average of the monthly fields.

Following Sallée et al. (2010), $S^{ox}$ was computed by considering that $H_{max} = H_{ml} + H_{sth}$, where subscripts $ml$ and $sth$ denote the seasonal ML and the seasonal thermocline respectively (Figure 1). Since $H_{max}$ is fixed over the annual cycle, the decomposition of the lateral induction term in Eq. 1 (similarly applied to the eddy-induced term) becomes:

$$\overline{[O_2]} \cdot \overline{U} \cdot \nabla_h \overline{H} = \overline{[O_2]}_{ml} \cdot \overline{U_{ml}} \cdot \nabla_h \overline{H_{ml}} + \overline{[O_2]}_{sth} \cdot \overline{U_{sth}} \cdot \nabla_h \overline{H_{sth}} \quad (2)$$

This method takes into account the seasonal variation of the surface $[O_2]$ and the different $U$ and $U^*$ in the two layers whose respective thickness vary seasonally. In the case of obduction, we considered the $[O_2]$ below the deepest ML base. The uncertainty associated with the sparse oxygen sampling and the interannual variability of oxygen and subduction is discussed in the supplementary material (Figures S3, S4).

### 3.2 Data

All the physical variables were obtained from the reanalysis produced by the consortium for Estimating the Circulation and Climate of the Ocean (ECCOv4 r3) (Fukumori et al., 2017). We have used climatological monthly mean values averaged over 1992-2015 with horizontal resolution of 0.5°x0.5°. The vertical grid spacing increases from 10 m near the surface to 457 m near the ocean bottom.

To validate the results obtained with ECCOv4, we computed the kinematic $S^{ox}$ using the gridded Argo product "In situ Analysis System" (ISAS15) (Gaillard et al., 2016; Kolodziejczyk et al., 2017). The resulting fields are available in the supporting information and show a good agreement (Figure S2).

The monthly climatological dissolved oxygen data were obtained from the World Ocean Atlas 2018 (WOA18) (Garcia et al., 2019), which provides statistical and objectively analysed data fields at 1°x1° resolution. All measurements used in this database have been obtained through the Winkler titration method. The oxygen field was then interpolated

onto the ECCOv4 grid. The WOA18 climatology contains data from 1955 to 2017. The different time window used to compute WOA18 and ECCOv4 climatologies constitutes a source of uncertainty.

# 4 Results

## 4.1 Geographical distribution of oxygen subduction

The largest oxygen fluxes into the thermocline are located (i) in the Southern Ocean (37%), with maximum to the east of Drake Passage and (ii) in the northern North Atlantic (30%), particularly in Labrador, Irminger and Nordic Seas (Liu & Huang, 2012). The Barents Sea constitutes an isolated hot-spot of oxygen uptake (Figure 2e) within the Arctic Ocean. In addition, we can identify weaker, but homogeneous subductive regions shaped by the subtropical gyres in every ocean basin. The majority of the $O^{ox}$ occurs in three regions: around 45% takes place in the Southern Ocean, around 22% in the subtropical-subpolar North Atlantic and 14% in the equatorial strip.

The $S^{ox}$ is globally shaped by the lateral induction (Figure 2a), the component with the highest magnitude located in well defined hot-spots. Nonetheless it produces a global net deoxygenation (-142 $Tmol\ yr^{-1}$). Lateral induction is driven by large MLD gradients in combination with strong regional currents (Figure S1b). It is maximum in the northern North Atlantic (Labrador and Irminger and Nordic seas) and in the Southern Ocean. The latter, driven by intense Antarctic Circumpolar Current (ACC) (Figure S1b). In the subtropical-subpolar North Atlantic, the Gulf Stream and the North Atlantic Current act as dynamical barriers; weak oxygen uptake occurs to the southeast, while intense $O^{ox}$ extends northeastward from the Florida Strait to the Norwegian Seas (Figure 2d)(Marshall et al., 1993; Qiu & Huang, 1995).

The eddy-induced term (Figure 2b), plays a role in the $S^{ox}$, especially in the North Atlantic and the Southern Ocean (Sallée et al., 2010; Portela et al., 2020). However, the main contributor to the ocean oxygenation is the vertical velocity (299 $Tmol\ yr^{-1}$). This term is relatively weak but homogeneously positive over the large extension of the subtropical gyres. Nonetheless, negative vertical velocity drives $O^{ox}$ near Antarctica and in the equatorial upwelling band where it dominates the total oxygen flux.

Oxygen diffusion, as found in other studies (Sallée et al., 2012; Kwon et al., 2016), is one order of magnitude smaller than the other terms at regional scale, but it is not negligible in the global integral. Diffusion estimations are uncertain since they are based on parametrisations. However, its vertical component is well represented in this study and, depending on the value of the lateral component, diffusion might be a key process for the ocean oxygenation. The vertical and lateral oxygen diffusion are shown separately in Figure S6 (supporting information).

To first order, mass and properties subducted into the ocean interior spread along isopycnals and the $[O_2]$ diminishes by mixing and biological consumption along the spreading path. The analysis of Apparent Oxygen Utilization (AOU= $O_{sat} - [O_2]$) sections across every ocean basin (Figure 3) can be seen as a proxy of the water-mass age (a reasonable assumption around the ML base (Brandt et al., 2015)) and it can trace back the main ventilation hot-spots in a way similar to the Lagangian approach.

Most obductive regions show relatively high AOU (Figure 3) which indicates that water has been subducted in remote locations and undergone mixing and biological consumption along its path. In the particular case of the North Atlantic, water subducted within the Subpolar Gyre in the Labrador Sea is transported into deep layers (>1000 m) while the water obducted further south, downstream of the main Gyre's flow has a different, less dense, subtropical origin (Figure 3c). However, the resolution of our computations does not allow

to elucidate if the oxygen subducted in the Irminger Sea experiences further reventilation and is re-subducted in the Labrador Sea (Figure S5) as suggested by (McCartney, 1982).

In the Indian and Pacific basins, recently subducted waters with low AOU are isopycnally transported and mixed northwards (Figure 3a, b,d). In these basins, Mode Waters (delimited by the two upper thick contours in Figures 3(a-c) are never reventilated, which results in increased AOU along their northward journey.

In the Southern Ocean (Figure 3d), well oxygenated waters are subducted near Antarctica during Bottom Water formation (Speer et al., 2000; Marshall & Speer, 2012). This feature, is not well captured in our $S^{ox}$ computation (Figure 2) but it leaves its signature with a relative deep AOU minimum deeper than 2000 m (Figure 3a-c).

### 4.2 Water-mass ventilation

The integrated effect of the $S^{ox}$ on isopycnals provides additional insight on the ocean (de)oxygenation during water-mass formation and erosion. As expected, the maximum oxygen uptake in every ocean basin occurs within the Mode Waters density range (Figure 4a-f) (Karstensen et al., 2008). Moreover, while Mode Waters density outcrops occupy 36% of the ML-base surface, they jointly account for 70% of the global oxygen uptake and they are dominant in every ocean basin (Figure 4f).

The intense oxygen uptake during Subantarctic Mode Water (SAMW) subduction occurs over a narrow density range in each Southern Ocean basin (Liu & Huang, 2012; Sallée et al., 2010; Portela et al., 2020).

In the northern North Atlantic, the outcropping isopycnals denser than 26.5 kg $m^{-3}$ undergo wide meridional excursions (Luyten et al., 1985) (Figure 2d). Due to that, the strong $S^{ox}$ detected at $\sigma$=27.8 kg $m^{-3}$ comprises both, the Subpolar Mode Water (SPMW) and waters of the Nordic Seas where strong deep convection and associated subduction occurs (Marshall, 1999). Half of the oxygen uptake in the Southern Ocean and the North Atlantic is tied to SAMW and SPMW formation (Figure 4f) which occurs within only 22% and 15% of the global outcropping density surface respectively. Hereinafter we will refer to the ensemble of these two mode waters as Subantarctic-Subpolar Mode Waters (SA-SPMW). This strong oxygen uptake during SA-SPMW formation is driven by lateral induction. The diffusion contribution is negligible with the reference diffusivity considered in this study but it could be important in the SA-SPMW density range with an enhanced $k_l$ value, as shown by the bars contours in Figure 4 (a-e).

The second peak of $S^{ox}$ corresponds to Subtropical Mode Waters (STMW). It is less intense, but extends over a greater density range than SA-SPMW (Figure 4). Particularly in the North Pacific ocean, oxygen subducted during STMW formation accounts for more than half of the oxygen uptake (Figure 4f). The $S^{ox}$ by STMW is driven by the vertical velocity (highlighted in Figure 4g), in majority explained by Ekman pumping (Qiu & Huang, 1995; Marshall et al., 1993).

The maximum $O^{ox}$ occurs (i) in the Southern Ocean, associated with the obduction mass flux that erodes the AAIW (Portela et al., 2020) driven by a combination of lateral induction and wind-driven vertical flux (Figure 4a-c) (ii) in the North Atlantic, driven by lateral induction (Figure 4e and (iii) in the equatorial strip (Figure 2c), where the wind-driven upwelling represents the zonal maximum of oxygen release (Figure 4g).

The spatial distribution of $[O_2]$, with the exception of the equatorial band, has a negligible effect on the global $S^{ox}$ which in turn is determined by the mass flux (Kwon et al., 2016). This is suggested by the small difference between $S^{ox}$ as computed from Eq.1 (filled area in Figure 4g), and that computed by assuming spatially homogeneous $[O_2]$ (black curve).

## 5 Discussion and Conclusion

The results presented here, show the mean state of the global $S^{ox}$. This is regulated by the physical mass flux while the spatial distribution of the $[O_2]$ at the ML base, linked to solubility effect, has a minor role (Kwon et al., 2016). In this study we provide a thorough description and the first quantification of the physical drivers of the ocean breathing. SA-SPMW are formed in hot-spots of intense lateral induction, while the wind-driven vertical velocity, although locally weak, dominates STMW subduction within the subtropical gyres. The percentage of oxygen that is globally subducted during mode water formation (70%) almost doubles that of the surface occupied by its outcropping isopycnals (36%) at the ML base. The enhanced contribution of mode water to the oxygen injection into the ocean interior corroborates their key role in ocean oxygenation.

Oxygen diffusion, a term often neglected (Kwon et al., 2016; Sallée et al., 2012) is locally small, but it becomes important in the global integral. The role of tidally-driven mixing in shaping the concentration of passive tracers in the open ocean has recently been highlighted by Tuerena et al. (2019). However, the choice of lateral diffusivity coefficients is largely uncertain and the diffusion contribution to the global oxygen uptake ranges from little to overwhelming. While the $k_v$ computed here is a reliable value, it is likely underestimated since it only considers the tidal mixing and it does not account for convective-driven mixing (Yeager & Large, 2007; Kolodziejczyk & Gaillard, 2013). A negative oxygen diffusion trend was found to be the dominant contributor of the predicted ocean deoxygenation over this century(Couespel et al., 2019). In line with these findings, our results underline the need to improve the global mapping of diffusion to fully understand the mechanisms of the ocean (de)oxygenation.

The Southern Ocean and the North Atlantic are the two lungs of the ocean. One third of the global oxygen uptake and nearly half of the oxygen release take place in the Southern Ocean. Moreover, the inter-basin exchange provided by the ACC is, at least, one order of magnitude larger than all the other inter-basin flows combined (Rintoul, 2000) which increases the potential of the Southern Ocean to provide oxygen to the rest of the ocean. The oxygen subducted in the Southern Ocean is distributed (i) to intermediate depths following SAMW formation (Portela et al., 2020; Kolodziejczyk et al., 2019; Hanawa & Talley, 2001) and (ii) to the deep ocean during the Bottom Water formation (Speer et al., 2000; Marshall & Speer, 2012; Rintoul, 2000). On the other hand, the Northern North Atlantic, following winter deep convection (Wolf et al., 2018; Körtzinger et al., 2004; Fröb et al., 2016), oxygen is provided to Circumpolar Deep Waters as part of the Atlantic Meridional Overturning Circulation (AMOC) (Lumpkin & Speer, 2007).

The strong obduction regions in the Southern Ocean have been substantially affected by deoxygenation over the past decades (Oschlies et al., 2018; Helm et al., 2011). This can be explained by an increase of the obduction rate in the Southern Ocean together with the stratification increase. The resulting reduced ventilation leads to a progressive substitution of relatively oxygenated waters by older waters with lower $[O_2]$ (Helm et al., 2011). This, in addition to the slowdown of the AMOC over the $20^{th}$ century (Rahmstorf et al., 2015) are consistent with the stronger global deoxygenation of deep waters (>1200 m) in comparison with those of surface and intermediate depths (Oschlies et al., 2018).

In this study, we investigated the $S^{ox}$ as the only physical mechanism leading to the injection of oxygen from the mixed layer into the ocean interior. While it is generally assumed that ocean mixing and air-sea oxygen fluxes prevent the retention of biologically produced oxygen in the ocean, it has been suggested that subsurface primary production makes a contribution to the oxygen flux in permanent stratified regions of the ocean as the Oxygen minimum zones (Richardson & Bendtsen, 2017).

$S^{ox}$ is critical for the long-term oxygen inventory. However, some of its components, like diffusion or eddy-induced subduction, are still uncertain and others, depend on the mixed layer depth, which show large variation between datasets (not shown). Thus, it is of key importance to reduce these uncertainties in order to better understand the global ocean deoxygenation and to improve the model estimations and forecasts. The results presented here provide new insights into the quantification of the physical contributors to the ocean breathing. However, the historical dissolved oxygen dataset is still sparse, and this prevents from obtaining a reliable global oxygen inventory and separating natural variability from long-term climate-related trend. Ongoing deployment of biogeochemical Argo global network including systematic oxygen measurements will bring new opportunities for investigating the global (de)oxygenation drivers and for monitoring the temporal evolution of $S^{ox}$ as well as the biogeochemical processes.

**Acknowledgments**

This study has been funded by the ACcOLADe LEFE/INSU project and E.P has been supported by a CNES/CNRS/Ifremer post-doctoral grant. The data used in this study are publicly available. ECCOv4 data can be obtained here: https://ecco.jpl.nasa.gov/drive/files. WOD18 oxygen data can be obtained here: https://www.nodc.noaa.gov/OC5/woa18/woa18data.html. ISAS15 is produced at LOPS as part of the Service National d'Observation Argo-France and made is freely available (doi:http://doi.org/10.17882/52367). The vertical diffusivity fields are available at https://www.seanoe.org/data/00619/73082/. We thank D. Couespel for valuable discussions on this subject and H. Regan for the English revision.

## 6 Author contributions

E.P and N.K conceived the idea of this study. E.P was the main writer of the manuscript and performed the computations with support from N.K. except for the diffusivity which was performed by C.V. All the authors participated in the analysis of the results and the writing of the manuscript in its final form.

## References

Abernathey, R. P., & Marshall, J. (2013). Global surface eddy diffusivities derived from satellite altimetry. *Journal of Geophysical Research: Oceans*, *118*(2), 901–916. doi: 10.1002/jgrc.20066

Bopp, L., Le Quéré, C., Heimann, M., Manning, A. C., & Monfray, P. (2002). Climate-induced oceanic oxygen fluxes: Implications for the contemporary carbon budget. *Global Biogeochemical Cycles*, *16*(2), 6–1–6–13. doi: 10.1029/2001gb001445

Bopp, L., Resplandy, L., Orr, J. C., Doney, S. C., Dunne, J. P., Gehlen, M., ... Vichi, M. (2013). Multiple stressors of ocean ecosystems in the 21st century: Projections with CMIP5 models. *Biogeosciences*, *10*(10), 6225–6245. doi: 10.5194/bg-10-6225-2013

Brandt, P., Bange, H. W., Banyte, D., Dengler, M., Didwischus, S. H., Fischer, T., ... Visbeck, M. (2015). On the role of circulation and mixing in the ventilation of oxygen minimum zones with a focus on the eastern tropical North Atlantic. *Biogeosciences*, *12*(2), 489–512. doi: 10.5194/bg-12-489-2015

Couespel, D., Marina, L., & Bopp, L. (2019). Major contribution of reduced upper ocean oxygen mixing to global ocean deoxygenation in an Earth System Model. *Geophysical Research Letters*, 1–23. doi: 10.1029/2019GL084162

Cushman-Roisin. (1987). Subduction. Dynamics of the Oceanic Surface Mixed Layer. In *Proc. 'aha huliko'a hawaiian winter workshop, honolulu, hi, university of hawaii at manoa* (pp. pp. 181–196).

de Lavergne, C., Vic, C., Madec, G., Roquet, F., Waterhouse, A. F., Whalen, C. B., ... Hibiya, T. (2020). A parameterization of local and remote tidal mixing. *Journal of*

*Advances in Modeling Earth Systems*. doi: 10.1029/2020ms002065

Donners, J., Drijfhout, S. S., & Hazeleger, W. (2005). Water Mass Transformation and Subduction in the South Atlantic. *Journal of Physical Oceanography*, *35*(10), 1841–1860. Retrieved from `http://journals.ametsoc.org/doi/abs/10.1175/JPO2782.1` doi: 10.1175/JPO2782.1

Forget, G., Ferreira, D., & Liang, X. (2015). On the observability of turbulent transport rates by Argo: Supporting evidence from an inversion experiment. *Ocean Science*, *11*(5), 839–853. doi: 10.5194/os-11-839-2015

Fröb, F., Olsen, A., Våge, K., Moore, G. W., Yashayaev, I., Jeansson, E., & Rajasakaren, B. (2016). Irminger Sea deep convection injects oxygen and anthropogenic carbon to the ocean interior. *Nature Communications*, *7*. doi: 10.1038/ncomms13244

Fukumori, I., Wang, O., Fenty, I., Forget, G., Heimbach, P., & Ponte, R. M. (2017). ECCO Version 4 Release 3. *Dspace.Mit.Edu*, *2*(2015), 10. Retrieved from `https://dspace.mit.edu/handle/1721.1/110380{\%}0Ahttp://hdl.handle.net/1721.1/110380` doi: 1721.1/110380

Gaillard, F., Reynaud, T., Thierry, V., Kolodziejczyk, N., & Von Schuckmann, K. (2016). In situ-based reanalysis of the global ocean temperature and salinity with ISAS: Variability of the heat content and steric height. *Journal of Climate*, *29*(4), 1305–1323. doi: 10.1175/JCLI-D-15-0028.1

Garcia, H. E., Weathers, K., Paver, C., Smolyar, I., Boyer, T., Locarnini, R., ... Reagan, J. (2019). WORLD OCEAN ATLAS 2018 Volume 3: Dissolved Oxygen, Apparent Oxygen Utilization, and Dissolved Oxygen Saturation. *NOAA Atlas NESDIS 83*, *3*(July), 38pp.

Gent, P. R., & McWilliams, James, C. (1990). Isopycnal Mixing in Ocean Circulation Models. *Journal of Physical Oceanography*, *20*, 150–155. doi: 10.1175/1520-0485(1990)020⟨0150:IMIOCM⟩2.0.CO;2

Gruber, N., Gloor, M., Fan, S. M., & Sarmiento, J. L. (2001). Air-sea flux of oxygen estimated from bulk data: Implications for the marine and atmospheric oxygen cycles. *Global Biogeochemical Cycles*, *15*(4), 783–803. doi: 10.1029/2000GB001302

Hanawa, K., & Talley, L. D. (2001). Mode waters. *Ocean Circulation and Climate: Observing and Modeling the Global Ocean*, 373–386 (736pp). Retrieved from `ftp://bslictb.nerc-bas.ac.uk/jbsall/Papers{\_}CMIP5team/2001Hanawa.pdf`

Helm, K. P., Bindoff, N. L., & Church, J. A. (2011). Observed decreases in oxygen content of the global ocean. *Geophysical Research Letters*, *38*(23), 1–6. doi: 10.1029/2011GL049513

Ito, T., Minobe, S., Long, M. C., & Deutsch, C. (2017). Upper ocean O 2 trends: 1958-2015 . *Geophysical Research Letters*, *44*(9), 4214–4223. doi: 10.1002/2017gl073613

Joos, F., Platiner, G. K., Stocker, T. F., Kortzinger, A., & Wallace, D. W. (2003). Trends in marine dissolved oxygen: Implications for ocean circulation changes and the carbon budget. *Eos*, *84*(21), 84–86. doi: 10.1029/2003EO210001

Karstensen, J., Stramma, L., & Visbeck, M. (2008). Oxygen minimum zones in the eastern tropical Atlantic and Pacific oceans. *Progress in Oceanography*, *77*(4), 331–350. doi: 10.1016/j.pocean.2007.05.009

Keeling, R. F., & Garcia, H. E. (2002). The change in oceanic O2 inventory associated with recent global warming. *Proceedings of the National Academy of Sciences of the United States of America*, *99*(12), 7848–7853. doi: 10.1073/pnas.122154899

Keeling, R. F., Körtzinger, A., & Gruber, N. (2010). Ocean Deoxygenation in a Warming World. *Annual Review of Marine Science*, *2*(1), 199–229. Retrieved from `http://www.annualreviews.org/doi/10.1146/annurev.marine.010908.163855` doi: 10.1146/annurev.marine.010908.163855

Klocker, A., & Abernathey, R. (2014). Global patterns of mesoscale eddy properties and diffusivities. *Journal of Physical Oceanography*, *44*(3), 1030–1046. doi: 10.1175/JPO-D-13-0159.1

Koelling, J., Wallace, D. W., Send, U., & Karstensen, J. (2017). Intense oceanic uptake of oxygen during 2014–2015 winter convection in the Labrador Sea. *Geophysical Research*

*Letters*, *44*(15), 7855–7864. doi: 10.1002/2017GL073933

Köhl, A., Stammer, D., & Cornuelle, B. (2007). Interannual to decadal changes in the ECCO global synthesis. *Journal of Physical Oceanography*, *37*(2), 313–337. doi: 10.1175/JPO3014.1

Kolodziejczyk, N., & Gaillard, F. (2013). Variability of the Heat and Salt Budget in the Subtropical Southeastern Pacific Mixed Layer between 2004 and 2010: Spice Injection Mechanism. *Journal of Physical Oceanography*, *43*(9), 1880–1898. Retrieved from `http://journals.ametsoc.org/doi/abs/10.1175/JPO-D-13-04.1` doi: 10.1175/JPO-D-13-04.1

Kolodziejczyk, N., Llovel, W., & Portela, E. (2019). Interannual variability of upper ocean water masses as inferred from Argo Array. *Journal of Geophysical Research: Oceans*, *i*, 1–19. doi: 10.1029/2018jc014866

Kolodziejczyk, N., Prigent-Mazella, A., & Gaillard, F. (2017). ISAS-15 temperature and salinity gridded fields. *SEANOE*. doi: https://doi.org/10.17882/52367

Körtzinger, A., Schimanski, J., Send, U., & Wallace, D. (2004). The ocean takes a deep breath. *Science*, *306*(5700), 1337. doi: 10.1126/science.1102557

Kwon, E. Y., Deutsch, C., Xie, S. P., Schmidtko, S., & Cho, Y. K. (2016). The North Pacific oxygen uptake rates over the past half century. *Journal of Climate*, *29*(1), 61–76. doi: 10.1175/JCLI-D-14-00157.1

Liu, L. L., & Huang, R. X. (2012). The global subduction/obduction rates: Their interannual and decadal variability. *Journal of Climate*, *25*(4), 1096–1115. doi: 10.1175/2011JCLI4228.1

Long, M. C., Deutsch, C., & Ito, T. (2016). Finding forced trends in oceanic oxygen. *Global Biogeochemical Cycles*, *30*(2), 381–397. doi: 10.1002/2015GB005310

Lumpkin, R., & Speer, K. (2007). Global ocean meridional overturning. *Journal of Physical Oceanography*, *37*(10), 2550–2562. doi: 10.1175/JPO3130.1

Luyten, J., Pedlosky, J., & Stommel, H. (1983). The ventilated thermocline. *Journal of Physical Oceanography*, *13*, 292–309. doi: 10.1007/BF02423489

Luyten, J., Stommel, H., & Wunsch, C. (1985). *A Diagnostic Study of the Northern Atlantic Subpolar Gyre* (Vol. 15) (No. 10). doi: 10.1175/1520-0485(1985)015⟨1344:adsotn⟩2.0.co;2

Marshall, J. (1999). OPEN-OCEAN CONVECTION: OBSERVATIONS, THEORY, AND MODELS. *Reviews of Geophysics*, *37*(1), 1–64.

Marshall, J., & Speer, K. (2012). Closure of the meridional overturning circulation through Southern Ocean upwelling. *Nature Geoscience*, *5*(3), 171–180. Retrieved from `http://dx.doi.org/10.1038/ngeo1391` doi: 10.1038/ngeo1391

Marshall, J., Williams, R. G., & Nurser, A. J. G. (1993). *Inferring the Subduction Rate and Period over the North Atlantic* (Vol. 23) (No. 7). doi: 10.1175/1520-0485(1993)023⟨1315:ITSRAP⟩2.0.CO;2

McCartney, M. S. (1982). *The subtropical recirculation of mode waters* (Vol. 40) (No. Supplement). Retrieved from `http://www.whoi.edu/science/PO/people/mmccartney/pdfs/McCartney82.pdf`

Munk, W., & Wunsch, C. (1998). Abyssal recipes II: Energetics of tidal and wind mixing. *Deep-Sea Research Part I: Oceanographic Research Papers*, *45*(12), 1977–2010. doi: 10.1016/S0967-0637(98)00070-3

Naveira Garabato, A. C., MacGilchrist, G. A., Brown, P. J., Evans, D. G., Meijers, A. J., & Zika, J. D. (2017). High-latitude ocean ventilation and its role in Earth's climate transitions. *Philosophical Transactions of the Royal Society A: Mathematical, Physical and Engineering Sciences*, *375*(2102). doi: 10.1098/rsta.2016.0324

Osborn, T. (1980). Estimates of the local rate of vertical diffusion from dissipation measurements. *Journal of Physical Oceanography*, *10*, 83–89.

Oschlies, A., Brandt, P., Stramma, L., & Schmidtko, S. (2018). Drivers and mechanisms of ocean deoxygenation. *Nature Geoscience*, *11*(7), 467–473. Retrieved from `http://dx.doi.org/10.1038/s41561-018-0152-2` doi: 10.1038/s41561-018-0152-2

Portela, E., Kolodziejczyk, N., Maes, C., & Thierry, V. (2020). Interior water-mass vari-

ability in the Southern Hemisphere oceans during the last decade. *Journal of Physical Oceanography*, *50*(2), 361–381. doi: 10.1175/JPO-D-19-0128.1

Qiu, B., & Huang, R. X. (1995). *Ventilation of the North Atlantic and North Pacific: subduction versus obduction* (Vol. 25) (No. 10).

Rahmstorf, S., Box, J. E., Feulner, G., Mann, M. E., Robinson, A., Rutherford, S., & Schaffernicht, E. J. (2015). Exceptional twentieth-century slowdown in Atlantic Ocean overturning circulation. *Nature Climate Change*, *5*(5), 475–480. doi: 10.1038/nclimate2554

Resplandy, L. (2018). Climate change and oxygen in the ocean. *Nature*, *557*, 314–315. doi: 10.1038/nature15216

Richardson, K., & Bendtsen, J. (2017). Photosynthetic oxygen production in a warmer ocean: The Sargasso Sea as a case study. *Philosophical Transactions of the Royal Society A: Mathematical, Physical and Engineering Sciences*, *375*(2102). doi: 10.1098/rsta.2016.0329

Rintoul, S. R. (2000). Southern Ocean currents and climate. *Papers and Proceedings of the Royal Society of Tasmania*, *133*(3), 41–50. doi: 10.26749/rstpp.133.3.41

Sallée, J. B., Matear, R. J., Rintoul, S. R., & Lenton, A. (2012). Localized subduction of anthropogenic carbon dioxide in the Southern Hemisphere oceans. *Nature Geoscience*, *5*(8), 579–584. Retrieved from `http://dx.doi.org/10.1038/ngeo1523` doi: 10.1038/ngeo1523

Sallée, J.-B., Speer, K., Rintoul, S., & Wijffels, S. (2010). Southern Ocean Thermocline Ventilation. *Journal of Physical Oceanography*, *40*(3), 509–529. Retrieved from `http://journals.ametsoc.org/doi/abs/10.1175/2009JPO4291.1` doi: 10.1175/2009JPO4291.1

Schmidtko, S., Stramma, L., & Visbeck, M. (2017). Decline in global oceanic oxygen content during the past five decades. *Nature*, *542*(7641), 335–339. Retrieved from `http://dx.doi.org/10.1038/nature21399` doi: 10.1038/nature21399

Speer, K., Rintoul, S. R., & Sloyan, B. (2000). The Diabatic Deacon Cell*. *Journal of Physical Oceanography*, *30*(12), 3212–3222. doi: 10.1175/1520-0485(2000)030⟨3212:tddc⟩2.0.co;2

Stramma, L., Johnson, G. C., Sprintall, J., & Mohrholz, V. (2008). Expanding oxygen-minimum zones in the tropical oceans. *Science*, *320*(5876), 655–658. doi: 10.1126/science.1153847

Tuerena, R. E., Williams, R. G., Mahaffey, C., Vic, C., Green, J. A., Naveira-Garabato, A., ... Sharples, J. (2019). Internal Tides Drive Nutrient Fluxes Into the Deep Chlorophyll Maximum Over Mid-ocean Ridges. *Global Biogeochemical Cycles*, *33*(8), 995–1009. doi: 10.1029/2019GB006214

Wolf, M. K., Hamme, R. C., Gilbert, D., Yashayaev, I., & Thierry, V. (2018). Oxygen Saturation Surrounding Deep Water Formation Events in the Labrador Sea From Argo-O2 Data. *Global Biogeochemical Cycles*, *32*(4), 635–653. doi: 10.1002/2017GB005829

Wyrtki, K. (1965). Surface Currents of the Eastern Tropical Pacific Ocean. *Inter-American Tropical Tuna Comission*, *9*(5), 271 – 304.

Yeager, S. G., & Large, W. G. (2007). Observational evidence of winter spice injection. *Journal of Physical Oceanography*, *37*(12), 2895–2919. doi: 10.1175/2007JPO3629.1

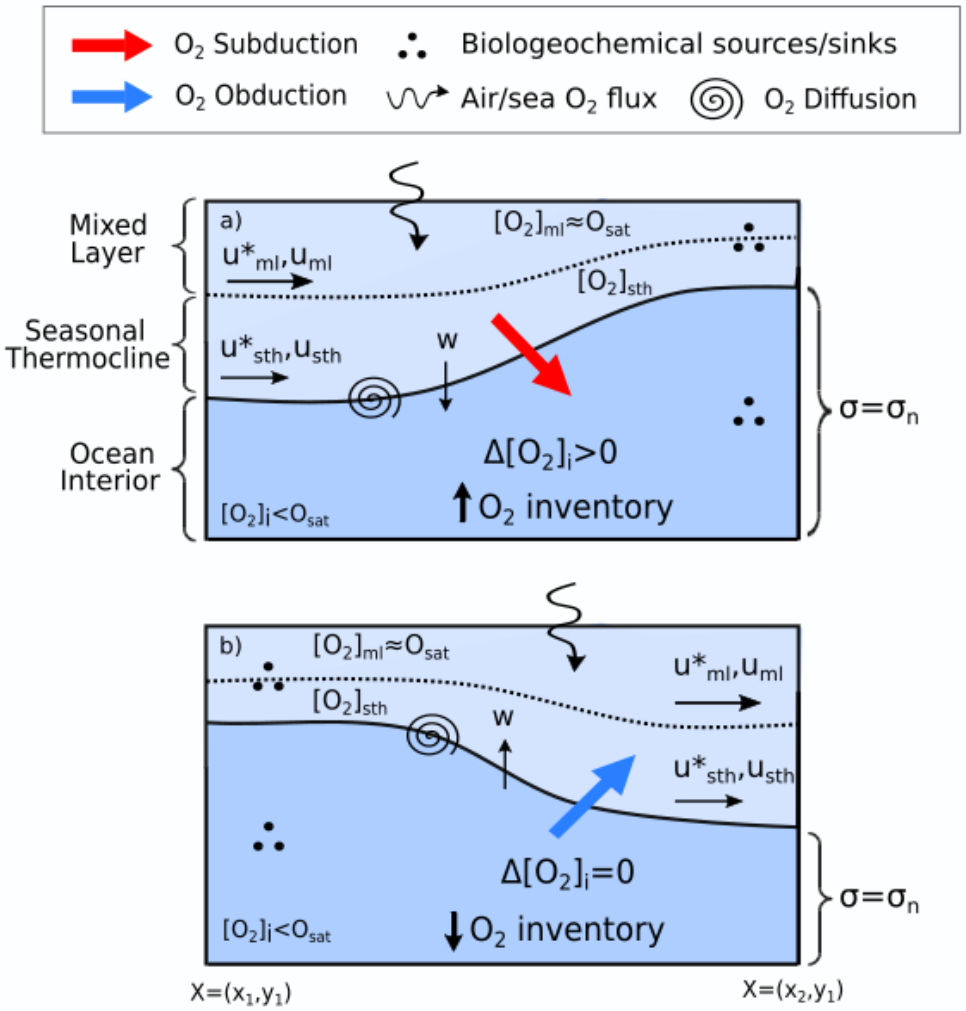


**Figure 1.** Schematic of the elements implied in a) $S^{ox}$ and b) $O^{ox}$ and their effect on the oxygen inventory and $[O_2]_i$ within a seawater volume confined between the steady late winter ML base and a variable density surface ($\sigma = \sigma_n$). Subduction brings oxygenated waters with $[O_2] \approx O_{sat}$ into the ocean interior which augments the interior oxygen inventory and the $[O_2]_i$. In contrast, obduction reduces the interior oxygen inventory due to the net volume loss, but the $[O_2]_i$ remains invariable. Subduction is computed by taking into account the different geostrophic and eddy velocity within the mixed layer ($ml$) and the seasonal thermocline ($sth$). Note that, for clarity, the $S^{ox}$ terms showed in the schematic point in the direction of the net flux, but different combinations are possible

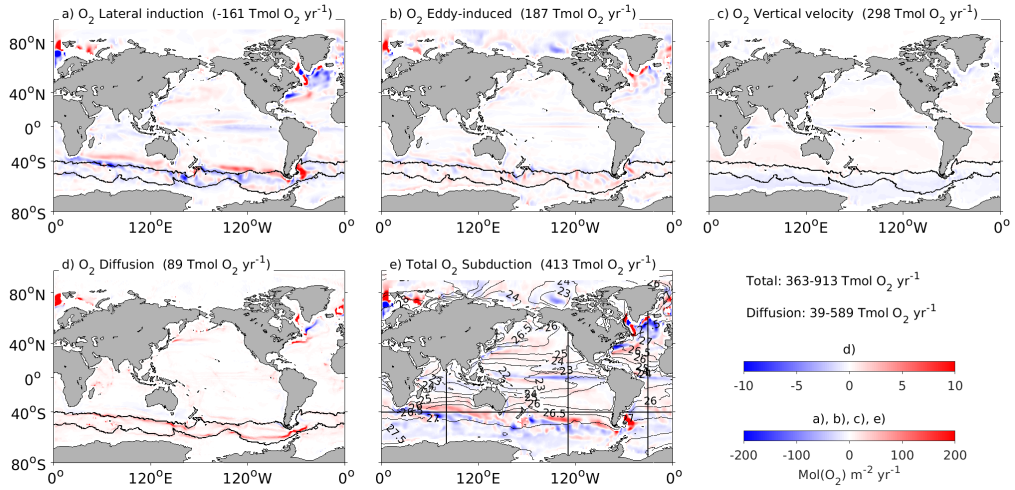


**Figure 2.** Spatial distribution of the $S^{ox}$ and its component terms. a) Lateral induction, b) eddy-induced, c) vertical velocity d) oxygen diffusion and e) Total $S^{ox}$. Note the different scale in d) which is one order of magnitude smaller than the other terms. Contours in (a-d) indicate the average limits of the ACC. Contours in (e) are the isopycnals at the deepest ML base. The straight lines in (e) indicate the position of the sections plotted in Figure 3. The globally integrated contribution of each term is indicated on panel's titles and the two extremes for diffusion and the total oxygen flux are shown on top of the colorbars

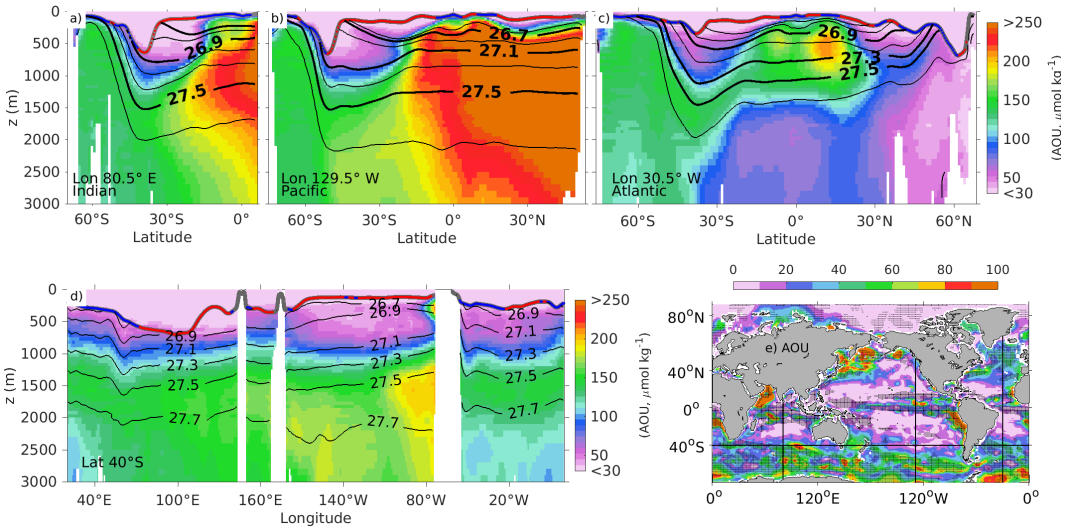


**Figure 3.** a-c) Mean meridional sections of AOU across the a) Indian b) Pacific and c) Atlantic oceans. d) Zonal section of AOU at 40°S. Black contours in a-d represent the mean position of the isopycnals from 26.5 kg m$^{-3}$ to 27.7 kg m$^{-3}$ and the thicker lines illustrate the SAMW and AAIW limits in every basin. The thick grey contour represent the deepest ML depth which has blue and red dots superimposed to indicate the subduction and obduction zones respectively. e) AOU at the late winter ML base. The stippling corresponds with obductive regions. The straight lines in e) represent the position of the sections.

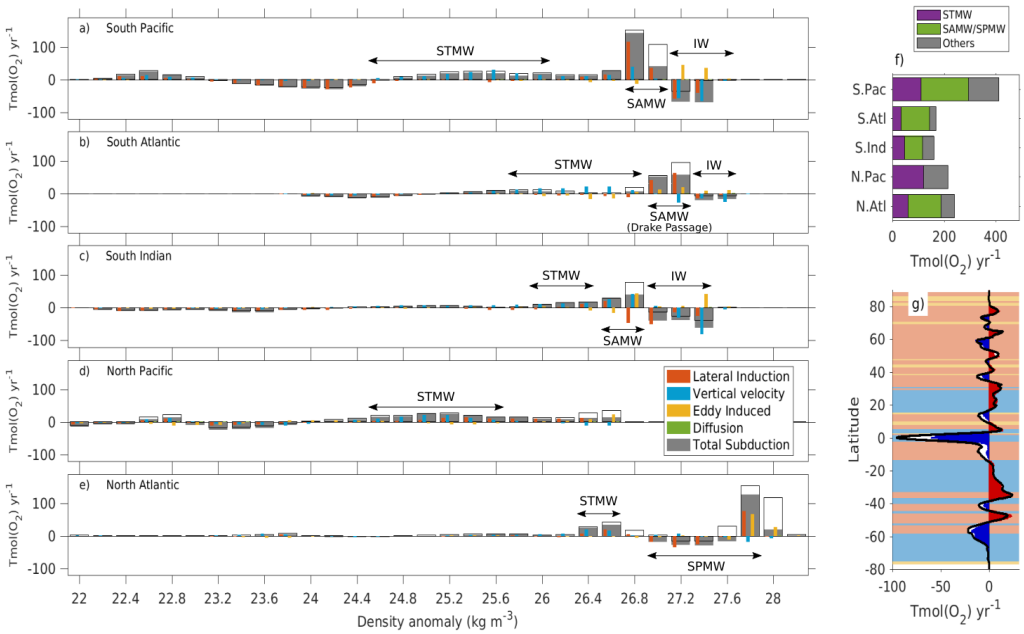


**Figure 4.** (a-e) Mean oxygen subduction rates and the contribution of each term by density class. The bars contour represent the total $S^{ox}$ with the maximum oxygen diffusion f) Contribution of the STMW and SA-SPMW to the total oxygen uptake in each basin. g) Zonal average of kinematic oxygen subduction rates where red (blue) colors indicate net $S^{ox}$ ($O^{ox}$). The solid black curve represents the zonal oxygen flux assuming an homogeneous spatial oxygen distribution (global average value). This curve demonstrates the small role that the $[O_2]$ distribution plays on the total $S^{ox}$. The background shading in g) shows the zonally dominant subduction component. The shading colors correspond to the legend in panel d)

# Supporting Information for: "Physical mechanisms driving the global ocean breathing"

**Esther Portela[1]*, Nicolas Kolodziejczyk[1], Virginie Thierry[1]and Clément Vic[1]**

[1]Univ. Brest, CNRS, IRD, Ifremer, Laboratoire d'Oceanographie Physique et Spatiale (LOPS), Plouzane, France

## S1 Mixed layer, current speed and oxygen distribution

The oxygen subduction ($S^{ox}$), is a complex mechanism resulting from the sum of different individual processes (Equation 1). In this section, to provide more insight on the drivers of $S^{ox}$, we show the average distribution of (i) the maximum mixed layer depth (MLD) at each grid point, (ii) the global horizontal current speed at the MLD and (iii) the oxygen concentration in equilibrium with the atmosphere ($O_{sat}$) (Figure S1).

The maximum MLD and the current speed are key factors for the lateral induction (Equation 1), which overall is the main driver of the total oxygen flux across the mixed layer base. Figure S1(a, b) shows how in the Southern Ocean there is a combination between MLD gradients and strong currents (the ACC) that explains the strong lateral induction. In contrast, in the North Atlantic, (in the Labrador and Irminger seas) and in the Nordic Seas, the currents are less intense than the ACC, but the MLD gradient is the largest of the entire ocean, resulting in the largest subduction rates.

The $O_{sat}$ distribution (Figure S1c) is largely driven by the temperature at the sea surface. Consequently, the largest $O_{sat}$ values are found at mid-high latitudes, together with the maximum $S^{ox}$. Nevertheless, the $[O_2]$ has shown to have a minor role in the total oxygen uptake which is dominated by the mass subduction flux across the mixed layer base.

## S2 Validation

To validate the results obtained with the reanalysis ECCOv4, we provide a plot of the total subduction and its three main components. The lateral induction and vertical velocity terms were obtained from the Argo-gridded product "In situ analysis System" (ISAS) (Figure S2)(doi:http://doi.org/10.17882/52367). ISAS is an optimal interpolated product of the Argo global data set that we used between 2006 and 2015, when the data coverage is globally satisfying. All variables are reconstructed on 152 depth levels ranging from 0 to 2000 m. Due to the impossibility to obtain consistent and reliable estimates of the bolus velocity from in-situ observations, we used the bolus velocity from the ECCOv4 outputs to compute the eddy-induced term showed in Figure S2. Since this term is not critical to the total $S^{ox}$ we consider our computation to be suitable for the validation purposes.

To compute the lateral induction from ISAS, we previously computed the geostrophic velocity field relative to 1000 m from hydrographic data. The mean reference velocity at that depth level, was obtained from ANDRO (doi:10.17882/47077), an Argo-based deep displacement dataset.

Corresponding author: Esther Portela, eportelanh@gmail.com

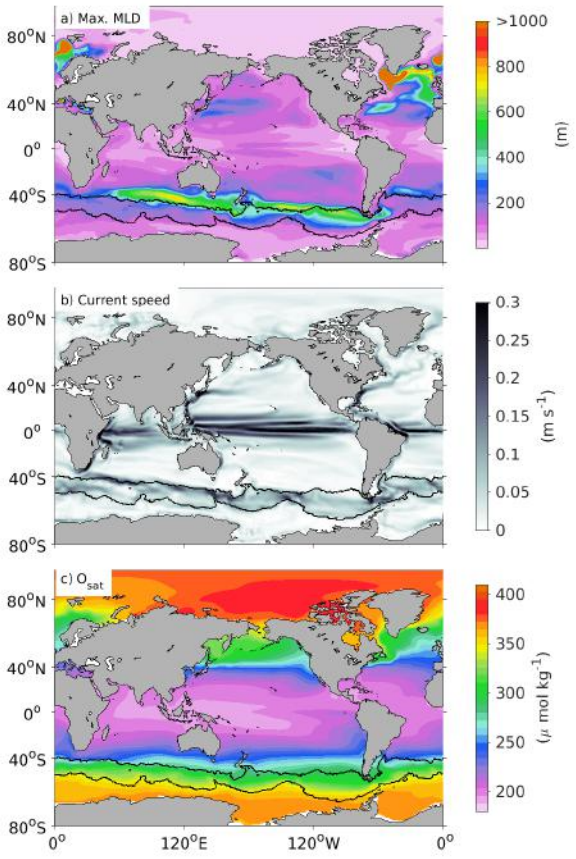


**Figure S1.** Fields related to the oxygen subduction. a) Maximum climatological MLD, b) Global geostrophic currents speed c) $O_{sat}$

Following (Marshall et al., 1993) The vertical velocity was approximated by using the linear vorticity balance (Sverdrup balance) as follows:

$$w_H = w_{Ek} + \frac{\beta}{f}\int_{-H}^{0} v dz \tag{1}$$

Where $w_{Ek}$ is the Ekman Pumping, $v$ is the meridional component of velocity and $\beta$ is the gradient of the planetary vorticity ($f$). Since the Ekman pumping cannot be computed within the equatorial strip, the surface between 5°S and 5°N was blanked.

Figure S2 shows a general agreement between the $S^{ox}$ as computed with both ECCOv4 and ISAS. The main differences are due to the small-scale structures that arise, mainly in the Southern Ocean in the $S^{ox}$ computed from ISAS. However, the main hot-spots and global features are well represented by both products with also similar magnitude.

## S3 Uncertainty Computation

Some sources of uncertainty were not considered in this analysis due to either the lack of the necessary elements to compute them or because of the little relative contribution that they have to the total error. The omitted error sources are the following:

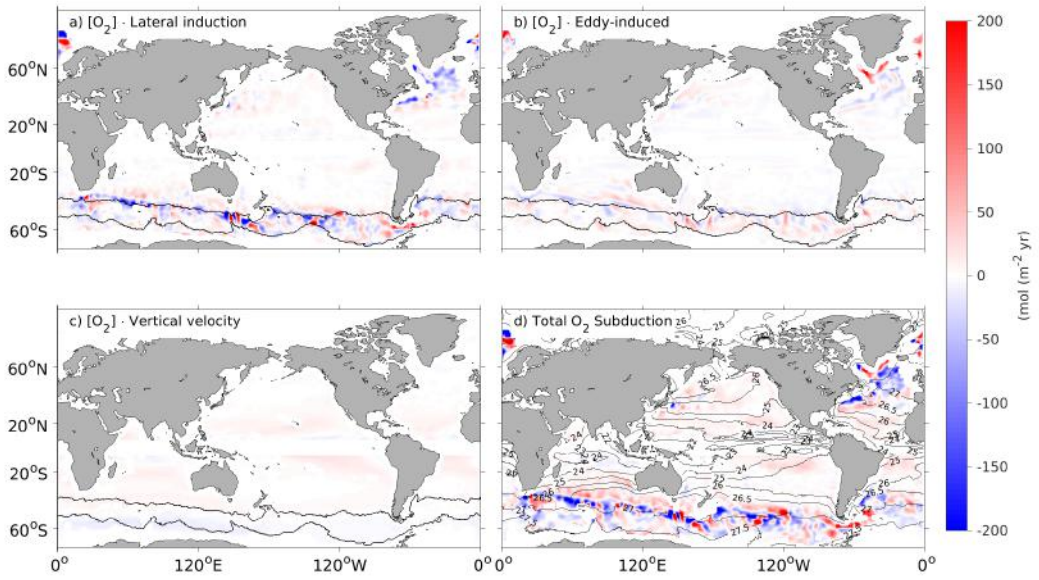


**Figure S2.** Oxygen subduction terms as computd from ISAS. a) Lateral ($O_2$) induction, b) ($O_2$) eddy-induced subduction computed from ECCOv4 bolus velocity, c) ($O_2$) vertical velocity and d) Total ($O_2$)subduction. Contours in a) indicate the mean ACC limits represented by the outermost closed streamlines through the Drake Passage. Contours in d) represent the mean position of the isopycnals on the deepest climatological MLD over the period 2006-2015.

1. In this study we have used two datasets which monthly climatology have different temporal coverage. While ECCOv4 extends from 1992 to 2015, the WOA18 oxygen climatology includes data collected from 1955 to 2018. This inconsistency is a source of uncertainty that we were not able to overcome and that needs to be taken in account for the interpretation of the results. However, due to the relative little role that the distribution of $[O_2]$ plays in the total $S^{ox}$ we consider that this uncertainty is negligible.
2. As the WOA18 data only uses oxygen data obtained by chemical Winkler titration methods, the error associated to the $O_2$-sensor calibration (critical in the CTD oxygen captors) is not considered in this study.
3. The error linked to the subduction computation will be neglected as it was performed from the ECCOv4 reanalysis outputs with no associated sampling or interpolation error.

In the following, we provide estimations on the uncertainty linked to the historically sparse oxygen sampling (Figure S3a, b), and to the interannual variability of the $[O_2]$ and the mass subduction flux. The interannual is the most important timescale non resolved by the monthly climatology fields used to compute $S^{ox}$, thus, it is thought to be a primary source of uncertainty. Finally we have propagated the error associated to each variable to obtain the final uncertainty linked to the $S^{ox}$ computation.

The oxygen data distribution shown in Figure S3a represents every single data collected between 1955 and 2018. We can see that the oxygen sampling has been historically uneven, typically, northern latitudes concentrate most of the data, mainly near the cost. The North Pacific and the northern North Atlantic count with approximately with four times more

data than the southern Hemisphere basins (Figure S3b) where observations are sparse. On the other hand, the distribution among density classes at each basin is acceptable suggesting that the relative contribution of the different water masses to the global oxygen uptake is well represented. Nevertheless, even if the whole ocean has been covered, the oxygen data are badly distributed which restricts the interpretation of the results of this, and any other study on oxygen at global scale.

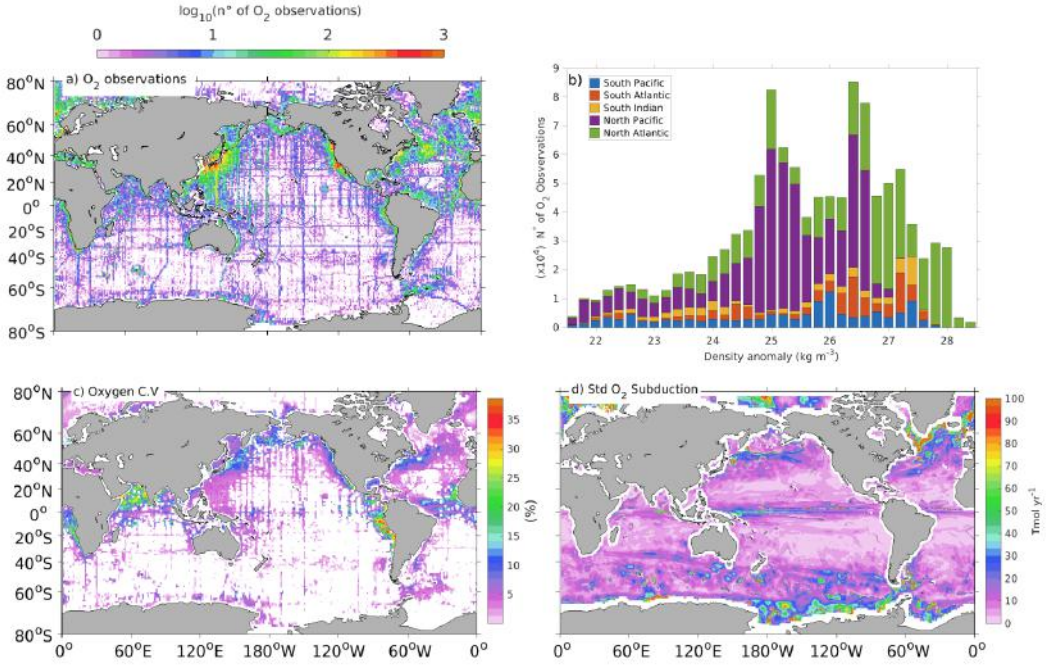


**Figure S3.** Uncertainty associated to the oxygen subduction components and to the oxygen sampling. a) . b) Number of historical oxygen observations contained in each density class and basin. c) Maps of the coefficient of variance (C.V, (%)) for the oxygen as obtained from WOA18. d) Map of the interannual standard deviation of the $S^{ox}$

The uncertainty associated to the interannual variability of the sparse oxygen data is expressed by the coefficient of variance (C.V. in %) of the $[O_2]$ (Figure S3c) (C.V $= 100 \cdot \sigma / \overline{x}$, where $\sigma$ is the standard deviation and $\overline{x}$ is the mean of all the available data within each grid cell between 1955 and 2018). The C.V allows to have an estimate of the data variability that is not affected by the mean value (with an equal C.V, locations with greater means will probably have larger standard deviations). Taking into account that the existing data cover more than 60 years the interannual variability of the $[O_2]$ is quite low. The maximum C.V reaches 40% only in very localized tropical regions,but globally, the interannual variability represents less than 15% of the mean value. In addition to the tropical regions as the North Indian and the eastern tropical Pacific, relatively high interannual oxygen variability is found in the North Pacific and subtropical North and South Atlantic. The C.V somehow reflects the data distribution (Figure S3a) but the blanked area is larger. This indicates that a big part of the ocean has been poorly sampled, making impossible the computation of the standard deviation. The Southern Ocean is one of the less sampled regions and it also shows low oxygen variability. Despite this results, due to the dominant role that the mass subduction flux plays on the total $S^{ox}$ we believe that the sparse oxygen sampling is a minor contributor to the total $S^{ox}$ uncertainty. The uncertainties associated to the interannual standard deviation of the $[O_2]$ and the mass subduction flux were propagated to

obtain the final standard deviation of the $S^{ox}$ following the typical equation of uncertainty propagation:

$$\sigma_{(S^{ox})} = |S^{ox}| \sqrt{\left(\frac{\sigma_{(O_2)}}{[O_2]}\right)^2 + \left(\frac{\sigma_{(Sub)}}{S}\right)^2 + \frac{2 \cdot cov([O_2], S)}{[O_2] \cdot S}} \quad (2)$$

Where $S$ is the mass subduction, $\sigma$ is the standard deviation of each variable, and *cov* is the covariance between the $[O_2]$ and the mass subduction. Assuming that these two variables are not correlated, the covariance term can be neglected.

The distribution of the uncertainty associated to the interannual $S^{ox}$ variability is shown in Figure S3d. The C.V was not used in this case since this metric does not work well for variables with values crossing zero as the $S^{ox}$. The distribution of the standard deviation of the mass subduction flux is not shown here because it approximates very much (only with different units) that of the $S^{ox}$. This indicates that the uncertainty of the oxygen flux across the mixed layer, as the $S^{ox}$ itself, is driven by the physical mass flux.

In the North Atlantic, the equatorial strip and within the ACC limits, high uncertainty (*i.e.* high interannual variability) is associated to intense mean $S^{ox}$ rates. The standard deviation represent between 30-50% of the mean value with local spots reaching the 100%. In contrast, this is not the case of the southernmost latitudes of the Southern Ocean where the high standard deviations could be explained by different factors: (i) it could represent actual interannual variability produced by the different ice coverage. (ii) it might reflect the relative scarcity of data constraining the ECCOv4 reanalysis in the highest latitudes and (ii) it could be due to the fact that the net $S^{ox}$ is nearly zero in this region. Given the impossibility of unraveling the source of uncertainty, it would be convenient to consider the $S^{ox}$ in this region carefully. Relatively high variability is also found in the Northern North Pacific, associated with the northern edge of the subtropical gyre.

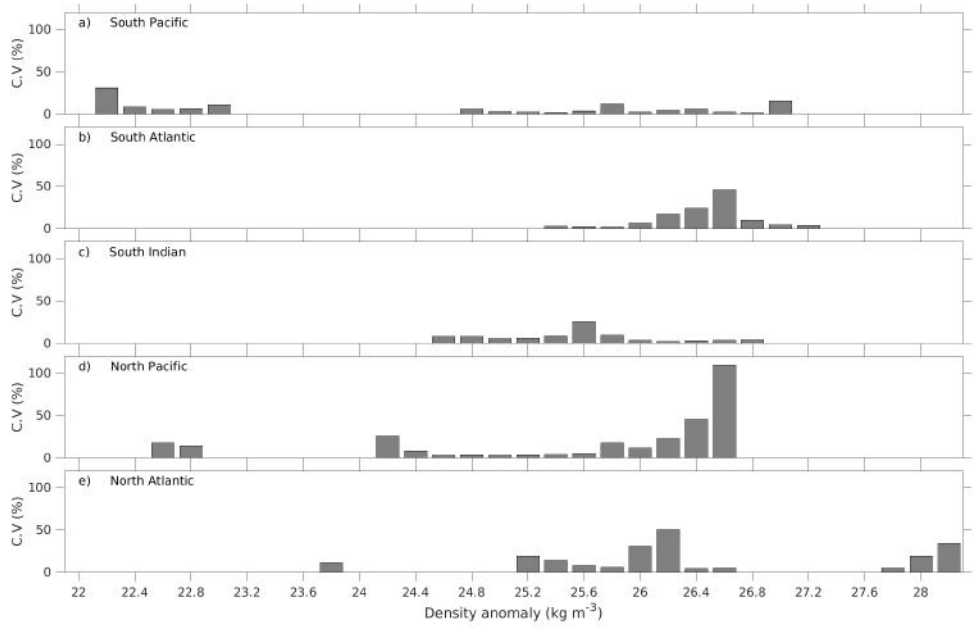


**Figure S4.** Coefficient of variation (C.V (%)) that illustrates the uncertainty due to the interannual variability of of the $S^{ox}$ and the sparse oxygen sampling for every density class and basin. Density classes with $S^{ox}$ lower than 1Tmol/Yr$^{-1}$ where not taken into account because their C.V results in abnormally high values

To link the reported uncertainty maps with our results, we show the C.V associated to the $S^{ox}$ integrated in density classes (Figure S4). To obtain the C.V, the standard deviation of the $S^{ox}$ as obtained from Equation (2) was propagated following the next equation:

$$[\sigma_m]_{(S^{ox})} = \sqrt{\sum_{i=1}^{n}(a_i^2 \cdot \sigma_i^2) + 2ab \cdot cov_{(i=1:n)}} \tag{3}$$

Where $\sigma_m$ represents the standard deviation within a given density class $m$, $a$ represents the area of each corresponding grid cell and $\sigma^2$ is the interannual $S^{ox}$ variance.

Here, we assume that the errors in the $[O_2]$ and the mass subduction have no spatial correlation. Then the covariance term is neglected and the error propagation associated to the integration in density classes can be expressed as the sum of the individual $S^{ox}$ uncertainties at every given grid point. We know that this assumption is incorrect, however, we do not have a reliable way to estimate the correlation scales and such assumptions have been made in similar studies. Given that limitation, we believe that the interannual variability in density classes showed here might be underestimated.

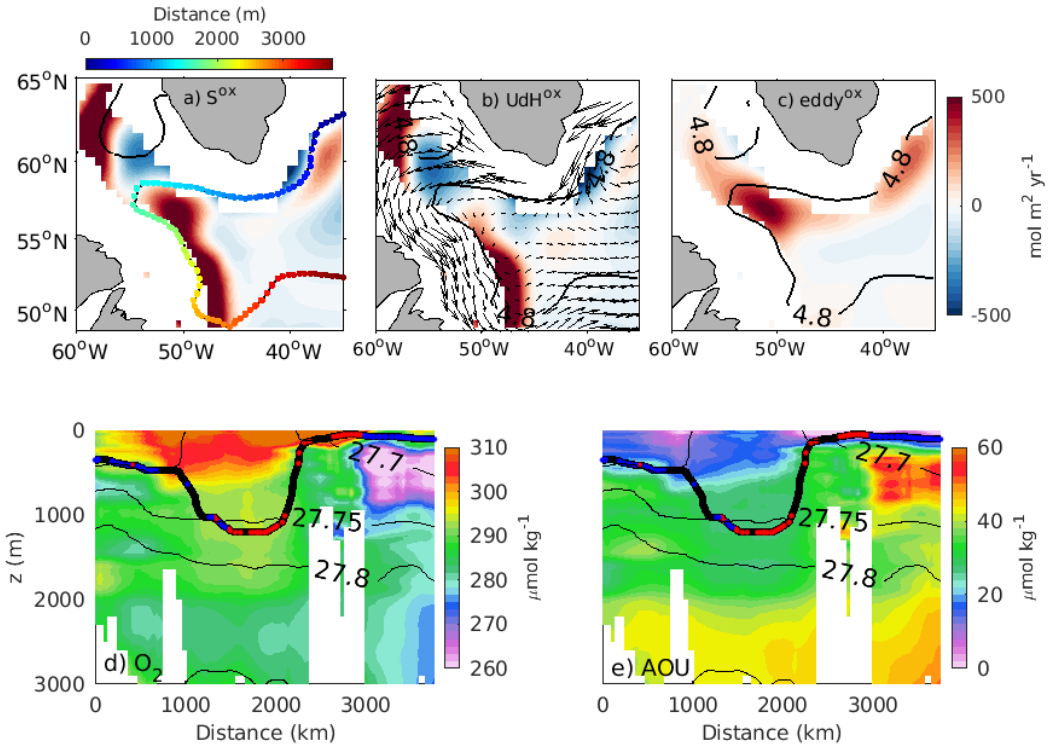


**Figure S5.** Sections following the circulation in the subpolar Gyre. a) $S^{ox}$ and the contour followed with distance color coded. b)$(O_2)$ lateral induction with the currents superimposed, c) $(O_2)$ eddy-induced subduction. d) oxygen and e) AOU sections. thin contours are the isopycnals while thick contour is the ML base. The colours (red and blue) on the ML base indicate the subductive and obductive regions respectively

Since the C.V expresses the percentage of variability as compared with the mean value, density classes with small mean $S^{ox}$ will result in abnormally high C.V. To avoid this artifact,

we have neglected the density classes with mean $S^{ox}$ smaller than 1 Tmol/Yr$^{-1}$. We can note that in most cases, the C.V do not overpasses 50% and that the largest uncertainties are not associated with the strong $S^{ox}$ fluxes. Instead, the maximum interannual variability is found in the northern North Pacific (>100%). High C.V. values are also associated with the STMW of the Atlantic Ocean and tropical waters in the Pacific Ocean.

## S4 Particular case of the Subpolar Gyre

Application of subduction concept to a regions were the large scale flow does not support the general shallowing of mixed layers in the direction of flow (As is the case of the Subplolar Gyre in the North Atlantic) pose a high degree of complexity to subduction estimates. To shed more light on the $S^{ox}$ in this complicated region, we show a section that follows a contourline along the circulation in the Subpolar Gyre (Figure S5)

## S5 Vertical and Lateral oxygen diffusion

Vertical oxygen diffusion was computed by using a geographically-variable vertical diffusion coefficient $k_v$ based on a parametrisation of tidally-driven mixing (de Lavergne et al., 2020). $k_v$ is determined at the base of the mixed layer.

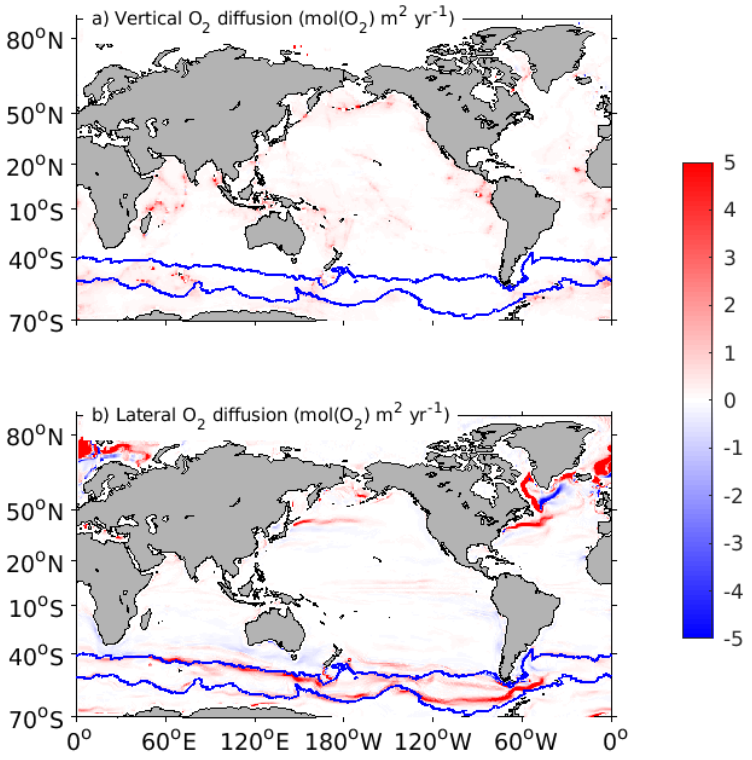


**Figure S6.** a) Vertical and b) lateral oxygen diffusion.

Lateral diffusion depends on data resolution and on the effect of eddies, it shows great variability between datasets and its magnitude is also related with that of the bolus velocity. In this study we used a constant mean value of the $k_l$ coefficient to compute the lateral oxygen diffusion showed in Figure S6

## References

de Lavergne, C., Vic, C., Madec, G., Roquet, F., Waterhouse, A. F., Whalen, C. B., ... Hibiya, T. (2020). A parameterization of local and remote tidal mixing. *Journal of Advances in Modeling Earth Systems*. doi: 10.1029/2020ms002065

Marshall, J., Williams, R. G., & Nurser, A. J. G. (1993). *Inferring the Subduction Rate and Period over the North Atlantic* (Vol. 23) (No. 7). doi: 10.1175/1520-0485(1993)023⟨1315:ITSRAP⟩2.0.CO;2